We are IntechOpen,
the world's leading publisher of
Open Access books
Built by scientists, for scientists

5,800
Open access books available

142,000
International authors and editors

180M
Downloads

154
Countries delivered to

Our authors are among the

TOP 1%
most cited scientists

12.2%
Contributors from top 500 universities

CLARIVATE ANALYTICS
BOOK CITATION INDEX
INDEXED

WEB OF SCIENCE™

Selection of our books indexed in the Book Citation Index
in Web of Science™ Core Collection (BKCI)

Interested in publishing with us?
Contact book.department@intechopen.com

Numbers displayed above are based on latest data collected.
For more information visit www.intechopen.com

Direct Energy Deposition of Cu-Fe System Functionally Graded Materials: Miscibility Aspects, Cracking Sources, and Methods of Assisted Manufacturing

Konstantin Makarenko, Oleg Dubinin and Igor Shishkovsky

Abstract

Direct energy deposition is a reliable additive manufacturing method of producing components with highly sophisticated geometry from a single material or combination of different materials with high manufacturing freedom and efficiency. The assembly operations are not required after the direct energy deposition: such complex parts as a rocket combustion chamber, a nuclear reactor element, a heat exchanger, and so on, could be fabricated layer-by-layer during one technological step. Promising applications are associated with Cu-Fe system laser deposited functionally graded components, which allow combining good oxidation resistivity, antifrictionality, thermal, and electrical conductivity of copper with mechanical strength, processability, and corrosion resistance of stainless steel. The main issue, which appears in the case of laser deposition of such materials, is internal stresses caused by significant inequality of physical properties of copper/bronze and steel, their limited miscibility, forming of brittle phases at the interface, and complexity of variation of mechanical and physical properties of the resulted alloy. The mentioned factors could cause various cracking in resulted parts. Specific techniques such as ultrasonic assistance, implementation of the external magnetic field, and post-treatment (hot isostatic pressing, machining), could be suggested to improve the quality of laser deposited Cu-Fe system functionally graded materials.

Keywords: direct energy deposition, functionally graded materials, Cu-Fe, Cu-Fe-Al, capillary convection, diffusion, cracking, ultrasonic-assisted DED, magnetically-assisted DED, hot isostatic pressing, machining

1. Introduction

Metal laser additive manufacturing (AM) includes a complex of precise rapid fabrication methods (selective laser sintering – SLS, also known as Direct Metal Laser Sintering™ – DMLS; selective laser melting – SLM, also known as laser

powder bed fusion – LPBF, and LaserCUSING™; direct energy deposition – DED, also known as laser directed energy deposition – LDED; laser metal deposition – LMD, direct metal deposition – DMD, Laser Engineered Net Shaping – LENS™, direct laser deposition – DLD, laser solid forming – LSF, laser metal deposition shaping – LMDS, and 3D laser cladding), which allows the creation of complex parts without assembly operations along with the low material waste. The AM also provides a possibility of in situ control and adjustment of process parameters for the better quality of the resulted parts using methods of laser-induced breakdown spectroscopy [1], acoustic emission sensors [2], machine learning [3], which allows the prediction of resulted phase composition and mechanical behavior of the parts, co-axial spatially integrated pyrometry [4], direct metal tooling [5], etc. The AM allows the fabrication of products not only from a single material but from a combination of two and more materials, which may have significantly different properties (such as alloys of Cu and Ni [6], Ni and Fe [7], Ni and Ti [8], Ti and Fe [9, 10], Cu and Fe [11, 12], Al and Fe [13], Al and Ti [14]). The resulted parts with the gradient of properties within their volume, created from various materials, are specified as functionally graded materials (FGMs) or compositionally graded materials [15–18]. The significant interest is attributed to the manufacturing of materials of the Cu-Fe system, which combine thermal expansion properties, electrical and thermal conductivity of bronze with high rigidity, mechanical strength (yield stress, ultimate tensile strength (UTS), flexure strength, creep resistivity), and corrosion resistance of stainless steel [19]. Moreover, the Cu-Fe alloys, especially multi-layered, are characterized by significant values of magnetoresistance [20–25]. The applicability of different AM technologies for Cu-Fe FGMs fabrication was justified by the results of the following research:

a. For the DED:

- X. Zhang et al. [26] successfully produced SS 304 L – commercially pure (CP) copper FGM with ~370% average thermal diffusivity and ~ 100% heat conductivity improvement in comparison with CP SS, through the intersections of a nickel-based alloy using the intermediate section technique [18];

- Authors of study [27] fabricated Cu-Fe FGM via the direct joining [18] with the resulted morphology of partially elongated columnar dendrites, and observed a microstructure refinement (up to 50 μm grain size) due to rapid solidification rate, but identified poor yield stress (123 MPa) and UTS (250 MPa), caused by the issues of direct bonding of such dissimilar materials;

- H.S. Prasad et al. [28] deposited a 99.9% CP copper on various metal substrates (aluminum, steel, and titanium) using a high-absorbable green (515 nm) disk laser source instead of common industrial infrared emitters. The longitudinal cracking in the case of steel-copper FGM was observed, and it was noted that the substrate preheating can be applied for the wettability of dissimilar materials improvement, which affects the resulted bonding parameters.

b. For other AM technologies:

- Y. Bai et al. [29] prepared the SS 316 L – C52400 metal composite via the SLM with two different interfaces (transition from SS 316 L to C52400

and vice versa) without any observable brittle intermetallics except CuNi;

- K.S. Osipovich et al. [30] fabricated the bimetallic samples from electrolytic tough pitch copper C11000 and SS 304 wire materials by the electron beam wire-feed AM technology with appropriate metallurgical bonding between SS and Cu with free of the defects transition zone.

The key difficulties with AM of Cu-Fe system FGMs are the stepping junction of Young's modulus of elasticity and coefficient of linear thermal expansion during the transition from Cu-based to Fe-based part; mismatch of the lattice parameters; poor mutual miscibility of steel and copper/bronze (especially during rapid solidification); embrittlement due to intermetallic phases forming [5]. The current study is devoted to the discussion of factors that have an influence on miscibility and intermixing in the liquid phase of Cu-Fe system alloys, possible sources of cracking of DED-fabricated Cu-Fe FGMs, and the assisted manufacturing techniques, which could be used for the improvement of the resulted parts quality.

2. Technological steps during the DED of FGMs, and miscibility aspects of the Cu-Fe system

The common process of the DED of FGM could be divided into several stages briefly described below.

a. Preheating of the substrate (optional; decreases the temperature difference between substrate and material, reduces stresses and strains in the resulted part, prevents warping and the separation from the substrate [31]);

b. Laser heating of the substrate along with heating and melting of the first particles of powder, which falls on the substrate and particularly absorbs the energy from the laser beam;

c. While the laser head moves in the X-Y coordinate plane, the new powder particles become heated and melted; simultaneously previous areas rapidly cool down and solidify;

d. When the first layer of the part is finished, the laser turns off, and the powder stream stops (it may take a small time delay between the shutdown of the laser and the moment when the last powder particles are thrown away from the powder nozzle by the feeding gas; thus, these particles can anyway sinter with the substrate or previous layer and cause satellite defects such as balled-up protrusion [31]. These defects could be eliminated by machining, or prevented by the proper scan path planning, appropriate terminations, and suitable powder delivery [31–33]);

e. Cooling time between layers: a process is paused for several seconds to let the previous layer(−s) cool down. On the one hand, it prevents overheating and re-melting of the previous layer(−s) (especially if they were fabricated from another material characterized by higher heat conductivity, higher laser radiation absorption, and lower melting point) and provides a more

appropriate thermal history (therefore, in some cases, the cooling time could be artificially increased to provide more intense cooling), but on the other hand, it could increase the further undesired thermal strains and stresses due to growth of the temperature gradient, and cause cracking. Besides that, it is significantly simpler to embed the new material inside the previously fabricated layers if they are preheated;.

f. The next layer is deposited on the previous, and the steps №№a)-e) are repeated; the difference from the first layer is that the heat is spread not only in the substrate but inside the previous layer(−s) too. Depth of the laser influence z, [m] in the case of laser-pulsed DED could be approximately estimated by the following Equation [34]:

$$z \simeq 2 \cdot \sqrt{\frac{a \cdot \tau_p}{\pi}} - \frac{T \cdot \kappa}{q}, \tag{1}$$

where τ_p, [s] is an average duration of the laser pulse; T, [K] is the temperature of the point with a coordinate z; q, [W/m^2] is a laser power density; a, [m^2/s] and κ, [W/(m·K)] are a thermal diffusivity and thermal conductivity of the material respectively (in the case of two or more component materials it is permissible, for a first approximation, to apply the rule-of-mixture equation to estimate the average a and κ of the complex system);

g. The fabrication of FGM by the transition from one material to another requires gradual modification of the powder chemical composition starting from the definite layer №n (smooth transitioning method), or beginning of the layer №n from completely new material (direct joining) [18]. In both these cases, a joint melt pool emerges, where both materials and the admixtures are distributed by two main mechanisms: capillary convection (Marangoni effect) and diffusion through the moving phase interface. It also should be mentioned here that the fluid motion in the melt pool could be also caused by the pressure of vapor, which evaporates from a front wall of the shallow vapor cavity [35], but this mechanism, associated with boiling, is common for several other laser treatment technologies such as laser cutting and laser alloying, but not relevant for the DED, where laser power is less than that is needed for boiling: $P < P_{boil}$. Therefore, two main mechanisms of intermixing, actual for the DED technology – a Marangoni effect and diffusion, are briefly specified below.

2.1 Marangoni effect

The capillary convection is associated with the movement of liquid near the phase interface caused by the dependence of surface tension on two factors – temperature and admixture concentration [35]: in particular, these parameters are different near the crystallization front and far away from it. Let us consider a horizontal layer of liquid with $\zeta < z < -h$ height ($\zeta \equiv 0$ if the liquid is not disturbed), which is heated from above by the source of concentrated energy like a laser beam, which is absorbed with the flow density Q. A temperature gradient dT_0/dz is constant. About 30 years ago, E.B. Levchenko and A.L. Chernyakov investigated, in this case, a propagation of heat- and mass-transporting capillary waves on the surface of nonuniformly heated liquid [36], and demonstrated that, using the linearized Navier–Stokes and heat conduction equations, supposing that liquid is incompressible, from the system of equations:

$$
\begin{cases}
\Delta\varphi = 0; \\[4pt]
\dfrac{\partial\vec{A}}{\partial t} = \nu \cdot \Delta\vec{A}; \\[4pt]
div\vec{A} \equiv 0; \\[4pt]
\dfrac{\partial T_1}{\partial t} + v_z \cdot \dfrac{dT_0}{dz} = \chi \cdot \Delta T_1; \\[4pt]
v = \nabla\varphi + rotA,
\end{cases}
\tag{2}
$$

with boundary conditions at $z = 0$:

$$
\begin{cases}
\rho \cdot \dfrac{\partial^2\varphi}{\partial t^2} - \alpha \cdot \left(\dfrac{\partial^2 v_z}{\partial x^2} + \dfrac{\partial^2 v_z}{\partial y^2} \right) + \rho \cdot g \cdot v_z + 2 \cdot \eta \cdot \dfrac{\partial^2 v_z}{\partial t \partial z} = 0; \\[8pt]
\dfrac{d\alpha}{dT} \cdot \left(\dfrac{\partial^2 T}{\partial t \partial x} + \dfrac{dT_0}{dz} \cdot v_z \right) = \eta \cdot \dfrac{\partial}{\partial t} \left(\dfrac{\partial v_x}{\partial z} + \dfrac{\partial v_z}{\partial x} \right); \\[8pt]
\kappa \cdot \dfrac{dT}{dz} = Q,
\end{cases}
\tag{3}
$$

and boundary conditions at $z = -h$: temperature $T = const$, velocity $v = 0$,

where φ and $\vec{A}$ are the scalar and vector potentials of velocity respectively, ρ, c, κ, and $\eta = \rho \cdot \nu$ are the density, specific heat, thermal conductivity, and viscosity of the liquid phase respectively, it could be shown that two wave types exist in the considered liquid:

- capillary-gravity waves:

$$
\omega_0 = \sqrt{g \cdot k + \frac{\sigma \cdot k^3}{\rho}}
\tag{4}
$$

- thermocapillary waves (sonic-type):

$$
\omega = k \cdot c,
\tag{5}
$$

where g is gravitational acceleration, k is a wave number, $c^2 \propto dT/dz$, σ is a surface tension coefficient. These two mechanisms (thermocapillary and capillary-gravity waves) are responsible for elemental intermixing at the interface area of FGM due to convection and have a significant influence on the resulting mechanical bonding strength.

The first factor of capillary convection – a dependence between surface tension and concentration – plays an important role in stimulating intermixing in binary systems such as Cu-Fe. If the expression for the molar Gibbs free energy of the multi-component liquid mixture is written in a form:

$$
g(T,P) = x_1 \cdot \left(g_1^0(T,P) + R \cdot T \cdot ln\, x_1 \right) + x_2 \cdot \left(g_2^0(T,P) + R \cdot T \cdot ln\, x_2 \right) + g^{ex}, \tag{6}
$$

where g^{ex} is an excess molar Gibbs energy of the liquid phase (could be defined using a Wilson equation), x_1, x_2 and $g_1^0(T, P)$, $g_2^0(T, P)$ are the mole fraction and molar Gibbs free energy at the temperature T and pressure P for components 1 and 2 respectively, and, assuming the equality of cross-interaction energy to the arithmetic mean of pure components 1 and 2, then the concentration-dependent surface tension of the liquid mixture σ_m (J/m^2) could be expressed as the following [37]:

$$\sigma_m = x_1 \cdot \sigma_1 + x_2 \cdot \sigma_2 - \left(\frac{x_1 \cdot x_2}{x_1 + x_2 \cdot a} \cdot b + \frac{x_1 \cdot x_2}{x_2 + x_1 \cdot c} \cdot d \right), \tag{7}$$

where σ_1 and σ_2, [J/m^2] are surface tension coefficients of the mixture components 1 and 2; a = Λ_{12}, b = R·T·$(\partial\Lambda_{12}/\partial A)$, c = Λ_{21}, and d = R·T·$(\partial\Lambda_{21}/\partial A)$ – adjustable parameters, different for various binary systems (A – surface area, [m^2], Λ_{12}, Λ_{21} – Wilson equation parameters). The Eq. (7) could be used for estimation of the surface tension for binary liquid mixtures and alloys but could be extended (in the general case) to the more complicated systems of three and more components, such as Cu-Fe-Al, Cu-Fe-Sn, Cu-Fe-Cr, etc., which are more relevant to the real FGMs.

Due to the second factor of the capillary convection – a temperature-dependent character of surface tension – the capillary convection has as much importance, so concentrated and narrow the energy source is [35]. The temperature depends on the coordinate along the part's surface, the absolute value of the surface tension in a liquid melt pool relies on the temperature of the surface and commonly decreases while the temperature grows. This gradient of the temperature (and the surface tension) is a source of a resultant force, which acts from the center of the laser heat spot to the periphery. If the surface is melted, this force initiates a movement of the liquid, which leads to an increase of intermixing between base material and admixtures – in the case of single-component alloy; between two base materials – in the case of Cu-Fe system alloys.

2.2 Diffusion

The diffusion through the moving phase interface (crystallization front) in the steady (quasi-stationary) process (while the admixture concentration in the solidified area is distributed regularly alongside normal to crystallization front) is described by the following Equation [19, 38]:

$$\frac{dC_l}{dt} = v_{cryst} \cdot \frac{dC_l}{dx}, \tag{8}$$

where C_l is an admixture distribution in the liquid phase near the crystallization front, v_{cryst} is a crystallization rate, t – time. If the process is unsteady (admixture concentration beside the crystallization front in the liquid phase is time-dependent), so the diffusion process in moving coordinate system $0x'$, associated with the crystallization front, will be described by the integral Equation [38]:

$$\frac{\partial C_l}{\partial t} = D \cdot \frac{\partial^2 C_l}{\partial(x')^2} + v_{cryst} \cdot \frac{\partial C_l}{\partial x'}. \tag{9}$$

This differential equation could be solved without significant difficulties in four different cases [38]:

1. Initial saturation during crystallization of the first portions of metal;

2. Quasistationary state;

3. Final saturation period, which happens when the last portions of metal crystallize;

4. Unsteady process – transient concentration variation, which appears when the crystallization rate changes.

The last case is the most suitable for the FGM fabrication via the DED, characterized by extremely non-equilibrium conditions. Therefore, the solution of the Eq. (9) in the fourth case via Laplas' integral transformation, is performed in consideration of three conditions [38]:

$$
\begin{cases}
C_l = C_0 \ if \ x' = \infty \text{for each } t \geq 0; \\
C_l = C_0 \cdot \left(1 + \dfrac{1-k}{k} \cdot exp\left(-\dfrac{v_{cryst}}{D} \cdot x' \right) \right) \text{for} \forall x' \geq 0 \text{ at initial time } t = 0; \\
D \cdot \dfrac{C_l}{\partial x'} + v_{cryst} \cdot (C_l - C_s) = D \cdot \dfrac{C_l}{\partial x'} + v_{cryst} \cdot (1-k) \cdot C_l = 0 \text{ if } x' = 0,
\end{cases}
$$

(10)

which describes the unsteady diffusion process occurring along with the immediate change of the crystallization rate from the value v_{cryst} to the new value v'_{cryst}, and the transition from the distribution attributed to v_{cryst} to the distribution associated with v'_{cryst}, could be expressed by the following equation:

$$
\frac{C_s(x_1)}{C_0} = 1 - \frac{1}{2} \cdot erfc \left(\frac{\sqrt{\dfrac{v_{cryst}}{D}} \cdot x_1}{2} \right) + (1-k) \cdot \left(\frac{\dfrac{v_{cryst}}{2 \cdot v'_{cryst}}}{k - \dfrac{v_{cryst}}{v'_{cryst}}} \right)
$$

$$
\cdot exp \left(-\frac{v_{cryst}}{v'_{cryst}} \cdot \left(1 - \frac{v_{cryst}}{v'_{cryst}} \right) \cdot \frac{v'_{cryst}}{D} \cdot x_1 \right)
$$

$$
\cdot erfc \left(\left(\frac{v_{cryst}}{v'_{cryst}} - \frac{1}{2} \right) \cdot \sqrt{\frac{v'_{cryst}}{D}} \cdot x_1 \right) +
$$

$$
+ \left(\frac{2 \cdot k - 1}{2} \right) \cdot \left(\frac{1 - \dfrac{v_{cryst}}{v'_{cryst}}}{k - \dfrac{v_{cryst}}{v'_{cryst}}} \right) \cdot exp \left(-k \cdot (1-k) \cdot \left(\frac{v'_{cryst}}{D} \right) \cdot x_1 \right) \cdot erfc \left(\left(k - \frac{1}{2} \right) \cdot \sqrt{\frac{v'_{cryst}}{D}} \cdot x_1 \right),
$$

(11)

where x_1 is a distance from the point, where the crystallization rate abruptly changed from v_{cryst} to v'_{cryst}, to the considered section, D is a diffusion coefficient, C_s is an admixture distribution in the liquid phase near the crystallization front, k is an admixtures distribution constant, C_0 is an initial admixture concentration, and erfc is a complement error function.

The diffusion processes commonly have a positive influence on the mechanical properties of as-deposited parts due to intensification of the intermixing, but the increase of a crystallization rate (what is common for laser technologies such as DED) leads to a decrease in the liquid alloy lifetime and lowers a diffusion intermixing in the liquid phase. Moreover, in specific Cu-I binary systems (where I = Fe, Co, Nb, Cr, and so on [39]), a liquid phase separation exists that prevents intermixing and makes difficulties for the desired alloy development. A discussion of this phenomenon along with parameters of temperature-and-concentration-dependent behavior of the material should be conducted using a Cu-Fe binary system phase diagram, which is demonstrated in **Figure 1** [20, 39–42].

As it was mentioned above, a Cu-Fe system is characterized by the existence of a metastable liquid miscibility gap [20, 39, 41–43] (binodal, or coexistence curve), which shows a specific transient temperature for each concentration of Cu and Fe: if the liquid is undercooled below this temperature (what is convenient for rapid solidification induced by laser treatment), a liquid separation of immiscible Cu and
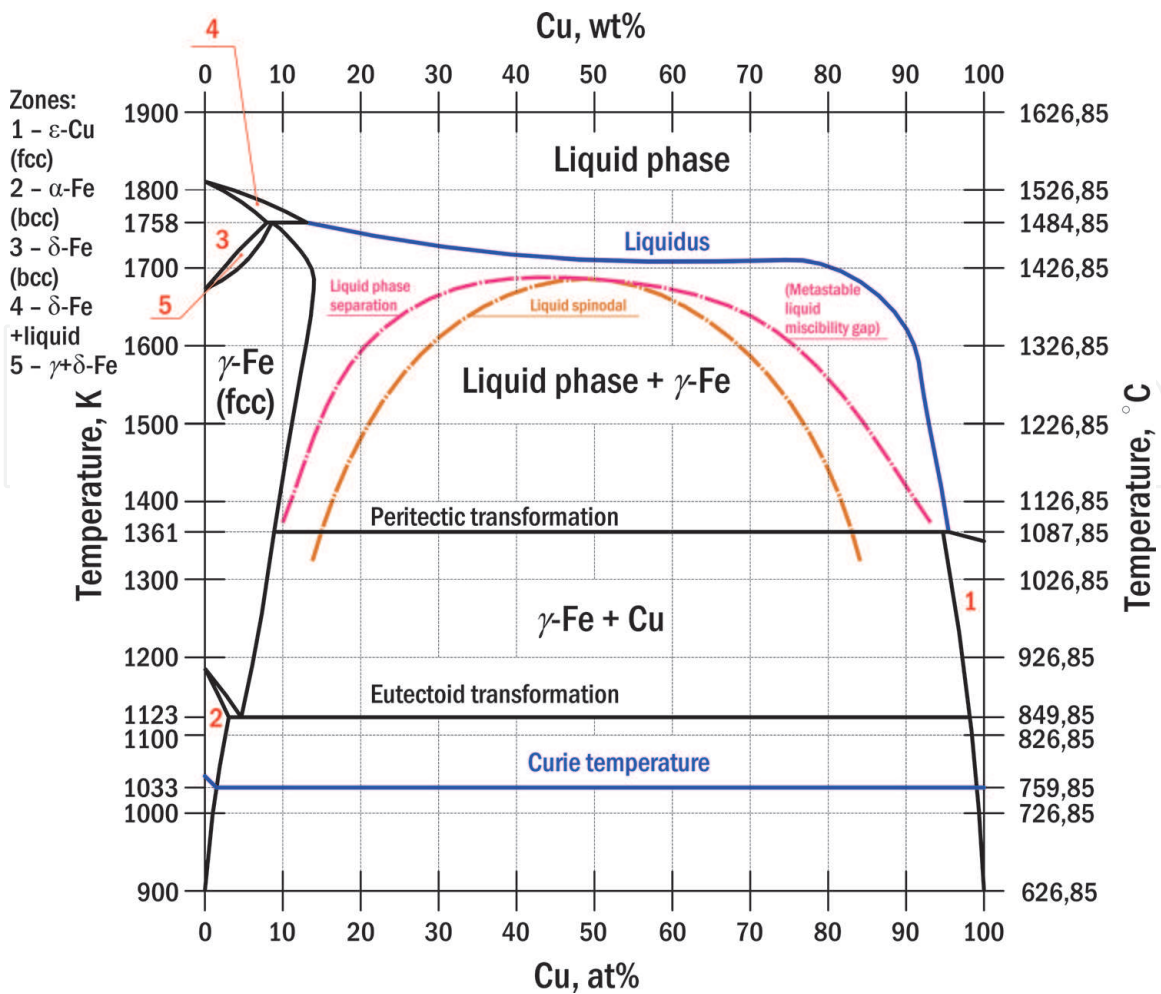
Figure 1.
A Cu-Fe system phase diagram [20, 39–42].

Fe appears [39], followed by further coagulation and dendritic crystallization after cooling. The position of this gap is shown by the pink line in **Figure 1**. A spinodal curve [42] (orange line in **Figure 1**) denotes the stable states, where such separation of undercooled liquid phases is not observed anymore (these states are located below this curve). The spinodal curve could be analytically described as a geometrical locus of points, where the Gybbs free energy second partial derivative with respect to concentration equals zero. The intersection point of these two curves (binodal and spinodal) is known as a critical point. Under that, a black horizontal line at the level of 1361 K shows the position of peritectic transformation (forming of an equilibrium solid solution consisting of a solid-state ε-Cu matrix around the γ-Fe dendrites, from the γ-Fe primary phase and surrounding liquid). The next line, associated with eutectoid transformation, corresponds to the temperature of 1123 K and shows a reversible disassociation of equilibrium solid solution into the two stable phases: α-Fe and ε-Cu. The Curie temperature of the Cu-Fe system equals to approximately 1033 K [39] (1043 K in the case of pure Fe [42]) (blue line in **Figure 1**). The Fe-rich areas of the phase diagram (located near its left side) are characterized mostly by face-centered cubic (FCC) crystal lattice; Cu-rich (right side) – by body-centered cubic (BCC). The phases observed at different temperatures and various Cu-Fe ratios are shown on the left top side of the diagram (and titled "zones") or are specified at the coordinate plane directly.

As it was said before, the existence of a metastable miscibility gap, caused by huge positive enthalpy between Cu and Fe, has a negative influence on the mechanical properties and applicability of Cu-Fe system FGMs [20]. The possible way of solution

Figure 2.
A 600°C experimental isothermal section of the Cu-Fe-Al system ternary phase diagram [44–46].

to this problem is a consideration of a ternary system Cu-Fe-X, where X is a third chemical element, which reduces the incompatibility of Cu and Fe by forming sustainable equilibrium phases, including the case of a high-speed solidification. Aluminum could be suggested as the possible example of this element according to the Cu-Fe-Al system ternary phase diagram shown in **Figure 2** [44–46]. The Cu-Fe-Al system has three established ternary phases: tetragonal $\omega FeCu_2Al_7$ (ω in **Figure 2**), stable icosahedral quasicrystalline $\tau_i FeCu_2Al_6$ forming between 750 and 800°***C*** (I in **Figure 2**), and $\varphi FeCu_{10}Al_{10}$ (φ in **Figure 2**), which forms in a solid-state and exists at 600°C [44–46]. In practice, such ternary system could be realized by using a SS – aluminum bronze FGM, which was discussed, for example, in studies [5, 19]. Other notations in **Figure 2**: B2 – ordered BCC phase, L – liquid phase, ε_2 – binary compound $\varepsilon_2 Cu_3Al$, δ – binary compound δ in the Al-Cu system, η_1 – binary compound $\eta_1 CuAl$, (Al) – solid solution based on disordered FCC Al phase, β' – phase-separated from the solution of FeAl in the ternary system [46].

3. Types of cracking in laser deposited FGMs and their sources

During the laser treatment processes, associated with the melting of metal (laser welding, laser cladding, DED, SLM, SLS), different types of cracking processes may appear. They are intensive in the case of the DED of Cu-Fe FGMs (especially at their interface areas [5]) because of the significant difference between physical properties, chemical compositions of base materials, and their limited miscibility, which was discussed above. Common cracking types include hot (solidification) cracking, liquation cracking, ductility dip cracking, cold cracking, and rewarming cracking (including post-weld heat treatment cracking). Below all these types of cracking and their sources are briefly described.

3.1 Hot cracking

Hot cracking, also known as solidification cracking, is a brittle intercrystallite (intergranular) failure, which appears along the boundaries of grains during the material crystallization [47, 48]. Elasticoplastic strains taking place during solidification cause hot cracking if their values exceed the strain capacity of the material [34]. One of the most significant parameters at this stage is a strain rate:

$$\alpha = \frac{\partial \varepsilon}{\partial T}. \qquad (12)$$

The thermophysical properties of base metals of the FGM, their rigidity, and the operation conditions determine a strain rate in the high-temperature range significantly. There is a specific temperature interval, where the plasticity and strength of both components of the FGM, or of one of them, are low; it is called a brittle temperature range (BTR) [34]. This interval is characterized by the decrease of plasticity and is the most probable for cracking. Overall, three factors play a leading role in forming of hot cracks:

1. Elasticoplastic strain rate;

2. BTR range;

3. Minimal plasticity of the material within BTR.

3.2 Liquation cracking

The liquation cracking is also a kind of intergranular failure, which occurs during solidification in the partially melted ("mushy") zones of the material because of grain boundary liquation [47–49]. This kind of cracking is the most common for Al-, Ni-, and Fe-based systems [49]. High thermal contraction of bronze and the presence of intermetallics provokes the increase of this type of cracking in the case of Cu-Fe system FGMs [47, 49]. Several works state that a high-energy input of the AM could also be a reason for the liquation cracking [50, 51].

3.3 Ductility dip cracking

The ductility dip cracking, associated with a local ductility loss, occurs between the different grains only in a solid-state of material [47, 49, 52, 53] in an elevated temperature range of $(0.5 \cdot T_{melt}) \lesssim T \lesssim T_{sol}$, where T_{sol} is a recrystallization (solidus) temperature (according to the other data – in a temperature range of about $0.4 \cdot T_{melt}$–$0.7 \cdot T_{melt}$ [50]). This type of cracking is actual for FCC alloys including Fe-, Ni- and Cr-based, but the systems that contain Cu also may suffer the ductility dip cracking: for instance, the Al-9Cu-6Ce (wt%)-based AM-fabricated alloys demonstrated the ductility dip at elevated temperatures ($\leq 400°C$), which was attributed to a concomitant dip in a strain-rate sensitivity of deformation [54]. It should be noted that as distinguished from the liquation cracking, the ductility dip cracking does not exhibit a liquation [49].

3.4 Cold cracking

Cracking that appears in the material during its cooling at $T \lesssim 473$ K or within several days after printing, is called cold cracking. Cold cracking has a character of a

slow failure. A long-time influence of the internal residual stresses causes elasticoplastic strain on the borders between different grains. Boundaries of grains have less stress resistivity compared with grain bodies because most part of the crystal lattice distortions is concentrated at the boundaries of grains [34]. Therefore, the most common areas of cold cracks appearance are the boundaries of the grains. Besides, further movement of a crack may include boundaries, such as the bodies of the grains. The high solidification rate, which is common for laser 3D printing, may provide intensification of many phase transformations in material, such as $\gamma \Longrightarrow \alpha$ transformation in stainless steel, and decrease the cold cracking resistivity. The grain refinement could contrarily increase this parameter (possible ways that lead to this result are discussed further in §4). Overall, the three most common sources of cold cracking could be specified:

1. Source №1 is a forming of the hard and brittle phases in the material during its solidification. If some regions gain low plasticity, high hardness, and increased specific volume (in other words, it may be said that these regions suffer full or partial hardening), their interface areas become saturated by internal stresses.

2. Source №2 is the existence of hydrogen (in several specific cases). Admixture of the hydrogen also may result in a cold cracking in the case of special kinds of steels or titanium alloys. The solubility of hydrogen in these materials strongly increases while the temperature grows. Therefore, the liquid metal during the DED may include a lot of hydrogen, which can be taken from the environmental gases. It is one of the reasons for the necessity of the shielding gas during the DED.

3. Source №3 is a combined source. The majority of cold cracks in the real cases (specifically of steels and titanium alloys) are provided by both sources simultaneously – the appearance of the low-plasticity phases along with filling with the hydrogen.

In the case of DED of Cu-Fe system FGMs, the cold cracks may be observed in three different regions of the FGM:

- in the steel area due to all three sources described before (hardening phases, which appear due to transformation of austenite to martensite, inclusion of hydrogen, or combined source);

- in the bronze area due to precipitation of hardening phases common for Cu-based alloys (β'-phase – a structured solid solution based on electron compound of Cu and Zn with BCC lattice – is more usual for brasses; Sn-enriched phases, such as $Cu_{31}Sn_8$; Pb-based phases); and the mixture of hydrogen or oxygen (the last one is the most undesired chemical element in pure copper or bronze) [34].

- in the border area if it consists of:

  ○ another material (in case of intermediate section method) – the source depends on the chemical composition of this material;

  ○ mixture of both materials (gradient path method) due to forming of the new brittle phases based on steel and bronze elements;

○ alternating layers of steel and bronze (alternating layers technique [5]) – the same as in the previous case.

If the border area is a narrow interface between steel and bronze (direct joining method), the most common types of cracking are hot cracks and liquation cracks.

3.5 Rewarming cracking

The rewarming cracking, which occurs due to cyclically repeated heating of the previously solidified layers is also a widespread source of cracking in the laser deposited FGMs, including Cu-Fe system alloys. The low laser radiation absorption coefficient of copper in the infrared area of the spectrum (which is common for the most part of commercially available industrial fiber lasers, such as erbium-dopped and ytterbium-dopped) could be the trigger for the fast-appeared rewarming cracking: the necessity of the high laser power implementation during the deposition of Cu-based layers leads to significant overheating of the volume of the part that lays beneath; the depth of such influence could be estimated using the Eq. (1). The slow-appeared rewarming cracking could appear during the heat post-treatment conducted after printing (post-weld heat treatment cracking) [50], such as high tempering, which is carried out under a DED-fabricated part to decrease its residual stresses. The rewarming cracking is characterized by its own BTR, which is lower than the BTR of the hot cracking and is commonly presented by the intercrystalline failure in the coarse-grained area of the part.

3.6 Summary

In the case of DED of Cu-Fe system FGMs, the most widespread types of cracking are hot, liquation, and rewarming cracking. Low-temperature cracking (ductility dip and cold) appears rather more uncommonly. The methods, which could be suggested to struggle with the cracking in these materials are:

• an increase of intermixing in the interface zones, which could be achieved by the implementation of several specific techniques such as ultrasonic-assisted manufacturing, which is described below in §4;

• grain refinement using such techniques as ultrasonic vibration assistance, magnetization of the melt pool by the external field, heat treatment (e.g. annealing) by the external laser source during the printing;

• decrease of microstructural defects such as porosity, shrinkage cavities, unmelted particles, and foreign inclusions, which could appear as stress concentrators (several methods of these parameters controlling are also discussed below in §4);

• exploitation of another laser sources instead of commercial fiber lasers (such as green disk solid-state lasers) with higher radiation absorption coefficient for Cu-based areas of FGM to decrease the excessive heat input into the material;

• realization of new experimental techniques such as hybrid laser-arc directed energy deposition;

- application of the intermediate section method to suppress a formation of brittle intermetallics, which could be also provoked by the increase of intermixing as its negative side effect;

- formation of stable phases during solidification by supplementation of additional constituents such as aluminum (see §2.2) and nickel (e.g. D22 alloy);

- improvement of the thermal history of the alloy by changing its fabrication process parameters;

- implementation of the alternating layers technique, which could be also suggested as an effective method of cracking reduction in Cu-Fe laser deposited FGMs.

4. Technological features for improvement of the DED-fabricated parts quality

In §§ 2–3 above, the aspects of miscibility and common sources of cracking in laser deposited FGMs, especially in Cu-Fe system, were described. Both these phenomena are linked to the mechanical strength of the resulted parts: an increased intermixing along with grain refinement commonly leads to a decrease in cracking, and vice versa: liquid phase separation and coarse-grained structure are factors of mechanical strength lowering, especially if they are followed by crystal lattice defects. Several specific techniques could be applied for increase of miscibility and decrease of cracking. The techniques are aimed to provide an increase in the quality of a) as-built DED-fabricated parts in situ; b) parts after the DED and post-treatment. The examples of valuable assisted manufacturing techniques are discussed specifically below.

4.1 In situ improvement of the DED-fabricated parts quality

4.1.1 Ultrasonic-assisted DED process

Our scheme of the ultrasonic-assisted DED is presented in **Figure 3**. The source of the ultrasonic frequency (~21 kHz) current signal (master oscillator in the scheme) is used for the generation of the mechanical wave inside the magnetostrictor (magnetostrictive transducer – a device that converts an ultrasonic frequency alternating current energy to the mechanical energy of ultrasonic frequency vibration) located in the stainless steel cooling reservoir. The wave is conducted to the waveguide, which is placed under the surface of the substrate with rigid fixation. In **Figure 4**, you can see our practical implementation of this scheme (left picture) and the resulted microstructure (right picture). The ultrasonic frequency generator UZG-2 M (is not shown in the picture) with 2 kW ultimate output power, 1.8–1.9 kW magnetostrictor PMS2–20 (pos. 2, placed in the Ø150x335 mm cylindrical stainless steel cooling vessel) with 21.5–22 kHz frequency range, and the titanium alloy waveguide (pos. 4) with rectangular base surface 120x18 mm were manufactured by OOO "Ultra-Rezonans" (Yekaterinburg, the Russian Federation). Water at room temperature was applied as a cooling liquid (2 L/min flow). The DED process was performed using InssTek MX-1000 3D-printer (InssTek, Daejeon, Republic of Korea) (pos. 1) in a direct tooling mode [5, 19] realized by two cameras (pos. 3). The microstructure image was obtained using an optical microscope Altami MET 1C (OOO Altami, Saint Petersburg, the Russian Federation). Pressing,
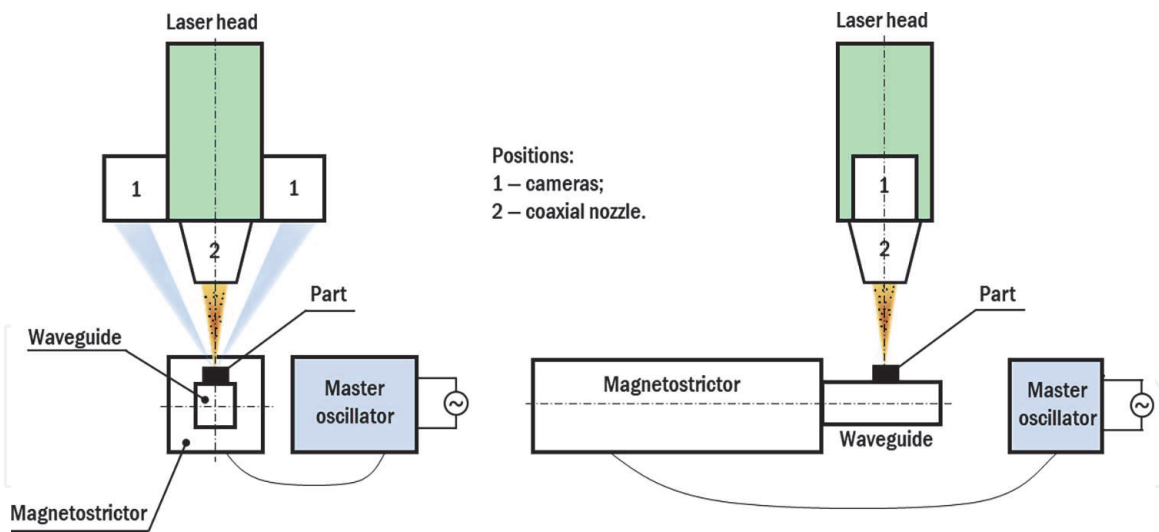
Figure 3.
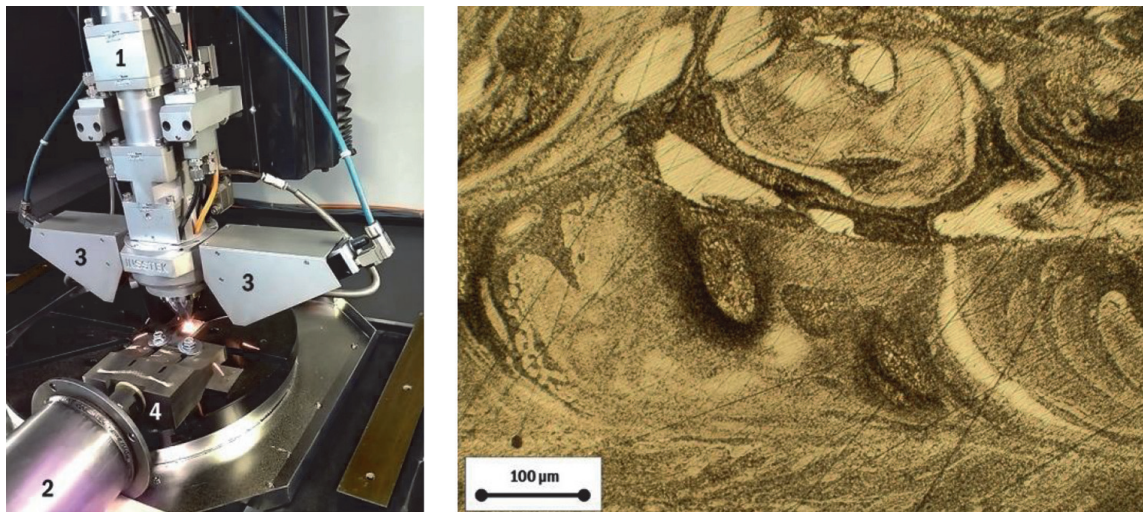*The ultrasonic-assisted DED process scheme.*

Figure 4.
The ultrasonic-assisted DED process. Left picture, positions: 1 – The laser head; 2 – The cooling vessel of the magnetostrictive transducer (see the description above); 3 – Cameras; 4 – Waveguide. Right picture: Example of the fine-grained intermixed microstructure of ultrasonic-assisted DED-fabricated part of 50% aluminum bronze with 9.5% Al and 1.0% Fe content (chemical composition similar to UNS C61800) and 50% SS 316 L. light areas: Islands of stainless steel, dark areas: The copper-based regions.

grinding, and polishing was conducted via TechPress 2™ and MetPrep 3™/PH-3™ (Allied High Tech Products, Inc., CA, United States) with 6 μm minimal grain size. The specimen was preliminarily etched for 9 s by 50 ml HCl + 50 ml C_2H_5OH + 2.5 g $CuCl_2$ [55–62].

The ultrasonic-assisted DED process is suggested to achieve the following advantages:

1. Refinement of the grain structure: X.H. Wang et al. [55] demonstrated the refinement of Fe-based composite coating after ultrasonic-assisted LMD, the disappearance of the columnar dendrites with 200 W ultrasonic power, and the appearance of the equiaxed dendrites with 400 W; C.J. Torado et al. [56] also observed the grain refinement of 3D-printed Inconel 625 using the ultrasonic assistance, decrease of the epitaxial growth and improvement of homogeneity.

2. Increase of microhardness and wear resistance: X.H. Wang et al. [55] showed that ultrasonic assistance increases the wear resistance of coating up to 2.4

times in comparison with a coating without ultrasonic assistance in the context of Fe-based composite LMD-fabricated coating deposited on the 5CrNiMo substrate. D. Zhang et al. [57] observed the increase of microhardness from ~380–450 HV1.0 to ~435 … 515 HV1.0 at all levels of laser output power due to grain refinement and reduction of the porosity. Method of strengthening of a part surface, an increase of average impact energy, hardness, a decrease of a wear mass loss, and redistribution of the reinforcement particles leading to their uniform dispersion, provided by the ultrasonic assistance, was also shown by the authors of the patent [58].

3. Increase of Young's modulus: D. Zhang et al. [57] showed that the ultrasonic vibration improves Young's modulus of the DED-fabricated parts from ~45–55 GPa to ~50–65 GPa.

4. Increase of the tensile strength: C.J. Torado et al. [56] pointed at the increase of tensile properties mostly due to the β-grain refinement: UTS with ultrasonic assistance was equal to ~1160 MPa (yield strength ~1100 MPa) while the results without ultrasonic assistance were: UTS ~1020 MPa, yield strength ~990 MPa (about 12% improvement of both parameters) of 3D-printed Ti-6Al-4V alloy. Y. Zhang et al. [59] achieved 1.4–1.6 times increase of tensile strength of Al 4047 parts due to grain refinement using the ultrasonic-assisted DED instead of traditional casting technology and observed the microstructure consisted of the columnar Al dendrites with equiaxed Si particles at boundaries of the layers along with equiaxed Al crystals surrounded by fine Si phases in the middle zone of the alloy.

5. Reduction of the eutectic spacing: S. Yan et al. [60] reported the decrease of this parameter in the carbon fiber toughening nanoscale Al_2O_3-ZrO_2 laser deposited eutectic, fabricated with ultrasonic assistance. The resulted value reached 50 ± 5 nm.

6. Improvement of the fracture toughness: S. Yan et al. [60] reported about 2.5–4 times increase in the carbon fiber toughening nanoscale Al_2O_3-ZrO_2 eutectic due to the grain refinement and the whisker toughening of the carbon fiber.

7. Removal of cracking: the authors of the patent [61] described the laser deposition of Al-12Si eutectic alloy and found out that cracking in the deposited structure, which was seen after the common DED, wasn't observed when the ultrasonic-assisted DED was implemented, and the microstructure of the sedimentary layer was changed.

Because of a serious lack of experimental studies related to the topic of ultrasonic-assisted DED of Cu-Fe system materials, it is struggling to predict indisputably that all the mentioned changes, described above, will be seen in the materials of this system too. Nevertheless, our first tensile tests of the binary Cu(50%)-Fe(50%) alloy (see **Figure 4** and its description) were conducted in accordance with ASTM E8/E8M-16a at 2.7 mm/min rate using INSTRON 5969 dual column machine showed that the average ultimate tensile strength of common DED-fabricated parts equals 848.3 MPa, while this result in case of the ultrasonic-assisted DED reaches 952.7 MPa, what is 1.12 times higher. Cu-based parts created from the tin bronze powder without any Fe-based constituents also demonstrate the responsiveness to the agitation of a melt pool by the ultrasonic frequency waves during the DED: A. Gorunov [62] observed the intermixing between the tin bronze clads and

material of a substrate along with substrate cracks bridging and claimed that it is possible to variate size, shape, and intermixing rate of the deposited material by changing the ultrasonic-related parameters of the process.

It is known that there is a dependence between mechanical performance and build orientation of parts fabricated via the traditional DED process. For instance, K. Zhang et al. [63] showed the difference between fracture morphology and anisotropic mechanical performance in specimens stretched parallel and perpendicular to the build direction; P. Guo et al. [64] reported that the higher elongation at failure was seen at 0° build direction rather than at 90°, what was an unexpected result because in the second case the direction of the external load was parallel to the dendritic grains; E. Azinpour et al. [65] observed the lower UTS and yield stress values of parts fabricated at 0° building direction in respect to the direction of load, in comparison with that of 90°. The build orientation of the part during the ultrasonic-assisted DED plays even a more important role in further mechanical characteristics, microstructure, and morphology parameters because of the significance of the mutual disposition between the ultrasonic wave front and the axes of the solidified grains of the material. Besides, the absorption of mechanical ultrasonic wave energy during its propagation within the volume of the part points to influence of a part's size and geometry on the ultrasonic-affected changes in its microstructural and mechanical properties. It is expected to observe a lower ultrasonic influence at the highest layers of a tall part if it is built in a vertical direction. Contrarily, if the part is a built-in horizontal direction, the ultrasonic influence will be more uniform and is expected to have a more regular distribution. The evaluation of ultrasonic attenuation in polycrystalline metals occurring mostly because of scattering from grains was conducted by T. Stepinski and P. Wu [66] for the pure copper specimens. A frequency-dependent attenuation coefficient $\zeta(f)$ was determined by the spectral shift method (based on the measurement of a signal reflected from the front and backs surfaces of the metal plate) using the following equation:

$$\zeta(f) = \left(\frac{2 \cdot \pi}{B}\right)^2 \cdot \frac{f_i - f_0}{2 \cdot D} \cdot f, \tag{13}$$

where B is the bandwidth of the input signal, f_i and f_0 are the central frequencies of the input and output signal respectively, and $2 \cdot D$ is a full path length of an ultrasonic signal (D – a thickness of the plate). The resulted measured attenuation amounted from $0.3684^{+0.0398}_{-0.0469}$ to $0.4613^{+0.0489}_{-0.0645}$ for 5.35 MHz central frequency in dependence on the specimen thickness (from 36 to 41.5 mm) and nominal grain size (from 125 to 175 to 250–350 μm). These results show that at the high frequencies the intensity of an ultrasonic wave in Cu polycrystal decreases by approximately 1.09–1.11 times per each mm propagated. Therefore, the Cu specimen even of a 40 mm height will suffer more than 30 times decrease in the ultrasonic wave intensity at its top surface at this frequency (5.35 MHz).

Besides, during our experiments, we observed that parts fabricated with ultrasonic assistance in a vertical build direction showed the defects increasing from the bottom to the top side (see the left picture in **Figure 5**). Nevertheless, the similar parts, fabricated at the same treatment regimes in a horizontal orientation, had a regular shape and normal roughness (**Figure 5**, middle picture). The same was shown by parts, deposited in a vertical direction without ultrasonic assistance (**Figure 5**, right picture). The increase in a surface roughness of the first part could be caused by a spatter due to significant vibration, or by the difference in the cooling rate of the lowest and the highest layers [31]. This difference comes from the fact that layers, larger affected by ultrasonic vibration, undergo more intense stirring provided by cavitation and acoustic flow effects [67] in a melt pool. The
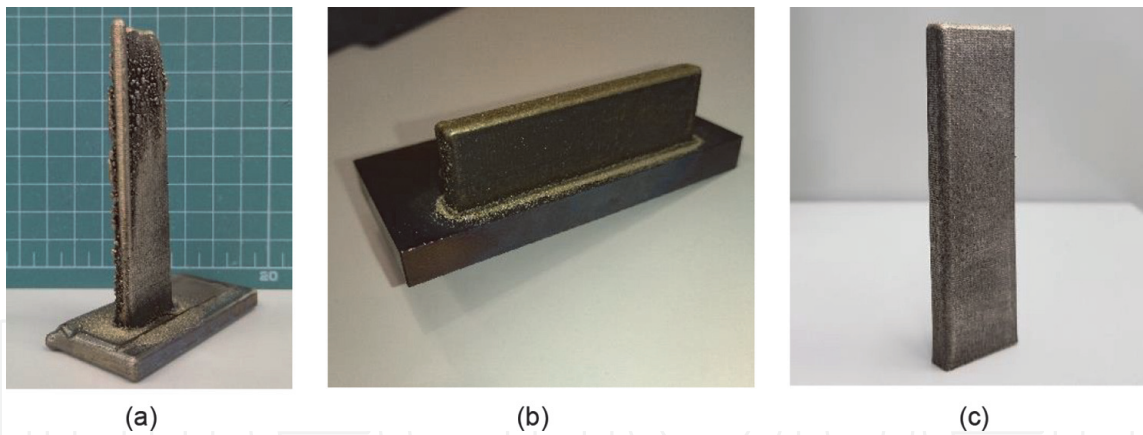
Figure 5.
Parts fabricated: a) with ultrasonic assistance (built in a vertical direction) (left picture); b) with ultrasonic assistance (built in a horizontal direction) (middle picture); c) without ultrasonic assistance (built in a vertical direction) (right picture).

cavitation effect is associated with nonlinearly expanding, contracting, oscillating, shrinking, and collapsing cavitation bubbles in liquid under alternating negative and positive pressure. The collapses of the bubbles produce instantaneous high temperature and pressure [68] in the surrounding area followed by the generation of high-speed liquid microjets and new bubbles nuclei keeping the ultrasonic cavitation process and promoting the liquid flow in the melt pool. The acoustic flow effect is a result of a sound pressure gradient caused by attenuation of the ultrasonic wave during its propagation in the melt. The sound flow slows down by reaching the bottom of the cavity, spreads upward along its side wall, and forms the circulation. The induced acoustic flow effect effectively promotes the flow in the molten pool, amplifying the effect of convection and diffusion.

The changes in the part's shape in its top section could appear because of a disproportional distribution of the powder due to vibration of the mounting layers and substrate. These defects were partially observed not only in parts fabricated via the ultrasonic-assisted DED, but the presence of ultrasonic vibration increased them. Columnar-shaped vertical tall deposit is seen only on the left side of the specimen because of the specificity of the track pattern: the path of the nozzle within each layer is finished near this area, therefore the last fallen powder particles are sintered to the hot surface even if the laser is already turned off. The mentioned defects could be reduced or eliminated by changing a part build direction, as it is shown in **Figure 5**, or a decrease of an ultrasonic generator output power.

4.1.2 Magnetization of the melt pool during the DED process

Magnetization of the melt pool by the external magnetic field during the AM processes, such as DED and SLM, could provide a slight change of phase distribution and intensification of iron oxidation [69] due to dominant thermoelectric magnetohydrodynamic convection. Other microstructural parameters of AM-fabricated parts could be also affected by the external magnetic field: J. Wang et al. [70] reported on the influence of the external magnetic field on the microstructure of laser deposited materials and observed a transformation from continuous to discrete morphology that was demonstrated for DED-fabricated SS 316 L. A similar transformation is also expected to be observed in Cu-Fe system SS 316 L-based FGMs, especially in the regions of the pure SS and mixture of SS and Cu/bronze. Then, D. Du, A. Dong et al. [71] discussed the increase of dendrite spacing and epitaxial nucleation of the laser deposited Inconel 718 alloy with the growth of the magnetic field flux density. The external magnetic field decreases the Marangoni

convection, so the forming of the equiaxed grains is suspended, and the growth of the columnar grain is increased, which is an undesirable property in most part of further practical applications, but this disadvantage is compensated by the formation of new equiaxed grains because of increase of the nucleation sites ahead of the dendrite front. Such an increase could also partially suppress the effects of liquid separation in Cu-Fe system FGMs and provide a slight increase in quality of as-fabricated parts. D. Du, J.C. Haley et al. [72] studied the influence of the external magnetic field on the properties of SLM-processed AlSi10Mg alloy, and observed a decrease of porosity, grain refinement and reduction of columnar grains, what approves a suggestion that the formation of new cellular dendrites prevails under the decrease of the amount of the equiaxed grain due to decrement of Marangoni convection, what was mentioned above. Grain refinement and increase of the amount of the equiaxed grain provide higher mechanical strength of the parts fabricated with the external magnetic field implementation, which was proved by the results of the mentioned study [72] (an increase of the UTS from 300 to 330 MPa to 390–410 MPa), but, nevertheless, wasn't demonstrated by A.M. Filimonov et al. [73] even with higher magnetic induction (0.2 T versus 0.12 T). It could point at the fact that this technique is not characterized by universality and could be applied for grain refinement and increase of the tensile strength in the case of specific groups of materials. The lack of experimental data does not allow us to evidently expect these phenomena in the case of Cu-Fe FGMs; therefore, this problem needs a more detailed experimental investigation.

Besides the increase of the mechanical strength, the quality of as-deposited parts could be enhanced via the magnetically-assisted DED by the improvement of the powder catchment efficiency leading to the better compression of fabricated tracks, a decrease of their skewness and dilution [74, 75]. If the ferromagnetic Fe-based powder is applied, these results could be also expected for Cu-Fe FGMs in the Fe-based area and regions with the presence of both Fe and Cu.

The practical interest of a magnetically-assisted DED approach in the case of Cu-Fe system is significantly associated with the formation of ferromagnetic phases in the material even it is fabricated from the non-magnetic initial components. The appearance of ferromagnetic BCC phase leading to 49 emu/g specific magnetizations of Cu-Fe binary alloy in presence of Al was shown by O. Dubinin et al. [76]. Similar magnetic properties were repeatedly approved by the authors of the current article during the investigation of the Cu-Fe binary alloy fabricated by the ultrasonic-assisted DED, which was discussed above in §4.1.1: the specific magnetization of this alloy amounted 58 emu/g (measured using the vibrating-coil magnetometer LakeShore 7410). Therefore, due to forming of ferromagnetic phases in Cu-Fe alloys, the external magnetic field is expected to have an influence on their parameters during the fabrication even there is no possibility to improve the catchment efficiency and variate the powder bed characteristics directly because of the utilization of the non-magnetic powders only.

The main disadvantage of the external magnetic field-assisted DED is expressed in the fact that, on the one hand, a low-power magnetic field could not provide significant microstructural changes [73, 69], and, on the other hand, the high-power fields have a negative influence on the components of a technological installation.

4.2 Post-processing treatment of the DED-fabricated parts

4.2.1 Hot isostatic pressing (HIP)

The part during a HIP is processed by the isostatic pressure of the confining inert gas in the high-temperature conditions [77]. The HIP post-processing is widely used

for porosity closing and homogenization of various metals (first of all, for Ti-based alloys) in casting, powder metallurgy, and AM [50], improvement of fatigue performance [77]. The volume fraction of the defects can be significantly reduced after the HIP, but nevertheless, several defects such as unmelted particles, porosity, and defects of the surface can be left after this post-treatment [78]. The phase structure could be changed and ductile phases such as α-martensite could be transformed into the ductile α–β phase [78] increasing the ductility of the processed part. For instance, P. Li et al. [79] reported the increase in cycle fatigue performance of LPBF-fabricated Ti-6Al-4V due to neutralization of the crack initiating defects under the part's surface.

The HIP could be also implemented for post-treatment of Cu-based AM-fabricated parts for enhancement of their physical properties [80] and quality. For instance, M. Agarwala et al. [81] applied the HIP for SLS-fabricated bronze-nickel alloy and showed that this technique allows achievement of the almost full-density parts with suppressed Kirkendall porosity, which is, due to the difference between a diffusion rate of Cu and Fe atoms, an important factor in a Cu-Fe system too (a self-diffusion coefficient of high-purity γ-Fe equals $0.18 \cdot \exp.(-64,500/(RT))$ cm^2/s [82], of Cu – $0.468 \cdot \exp.(-47,140/(RT))$ cm^2/s over the range 685–1062°C [83]).

However, the HIP of large-sized products, such as real space industry parts, requires huge technological installations, which is a limiting factor of this technique. The related industrial solutions include such examples as invention [84], technological installation [85], and large HIP systems [86].

4.2.2 Machining

Machining (including milling, turning, vibratory grinding, abrasive, chemical and electrical polishing, ultrasonic nanocrystal surface modification) of the DED-fabricated parts is a common process, which improves their surfaces' overall quality [87]. These techniques provide a decrease of the roughness of the laser deposited part surface and eliminate the satellite defects (such as protrusions), various edge defects (such as unsuitable levels of edges and their shape), and the morphological defects (such as waviness, blobs, and zits) [31]. Particularly for the Cu-based system, a magnetically driven abrasive polishing was implemented by I. Karakurt et al. [88] to improve the quality of electron beam melting-fabricated copper samples. The results showed a decrease in surface roughness from 35 μm to 4 μm. The Fe-based DED-manufactured material – A131 steel with a moderate percentage of copper (≤ 0.35 wt%) – was treated by the milling post-processing by Y. Bai et al. [89]: a significant surface roughness modification from >20 μm to <1 μm was gained, and the slight changing of microhardness was also observed. Nevertheless, the cracking, which is typical for the DED of Cu-Fe FGMs, as it was largely described above, is not expected to be eliminated by common machining techniques, which are mostly targeted to increase the overall surface quality and lowering of roughness.

5. Conclusion

In the current chapter, three interdependent aspects, important for the DED of Cu-Fe system FGMs, were observed: specificities of intermixing and miscibility; factors, leading to cracking; assisted manufacturing techniques, aimed at enhancement of the quality of the parts. It was pointed out that the typical FGM DED process could be divided into 7 stages, including the preliminary phase and the phase of the conjoining of the base metals A and B. The interfacial area between the

base metals A and B is characterized by the joint melt pool, where intermixing is dependent on two physical processes: capillary convection (including capillary-gravity waves and thermocapillary waves) and diffusion. The limited miscibility, precipitation of the hardening phases, excessive strain rates, porosity, unmelted particles, and other defects may cause cracking in Cu-Fe FGMs, especially at their interfacial area, which could be divided into the hot, liquation, rewarming, cold, and ductility dip cracking (three first types are prevalent). The limited miscibility between Cu and Fe could be improved by supplementation of a third component e.g. Al that provides forming of binary and ternary stable phases in the Al-Cu, Al-Fe, and Al-Cu-Fe systems, such as $\omega FeCu_2Al_7$, $\tau_i FeCu_2Al_6$, and $\varphi FeCu_{10}Al_{10}$. Using other laser sources (such as green disk solid-state lasers) with higher radiation absorption coefficient for Cu-based areas of FGM instead of commercial fiber lasers, it is possible to decrease the excessive heat input into the material. The specific technological approaches could be implemented for the DED-manufactured parts quality improvement, including the elimination of cracking. These approaches could be divided into two broad groups: techniques of the in situ influence, and the methods of post-processing. The ultrasonic-assisted DED and the DED in the external magnetic field were discussed specifically among the first group, the HIP, and the machining – among the second one. The ultrasonic assistance provides better intermixing, grain refinement, an increase in tensile strength, elasticity modulus, microhardness, fracture toughness, and wear resistance. The magnetically-assisted DED could also increase tensile strength, decrease porosity, refine the grain structure, improve the ferromagnetic powder catchment efficiency and compression of the tracks. The HIP provides homogenization and porosity closing (including the Kirkendall porosity), increasing the ductility and fatigue performance. The machining improves the overall surface quality of the parts, decreases roughness, eliminates satellite, edge, and morphological defects, e.g. waviness, blobs, and zits.

Acknowledgements

Author's contributions

Konstantin I. Makarenko: writing orignal manuscript, conducting experiments; Oleg N. Dubinin: conducting experiments; Igor V. Shishkovsky: providing guidance and revision.

Conflict of interest

The authors declare no conflict of interest.

Appendices and Nomenclature

AM   additive manufacturing;

BCC	body-centered cubic;
BTR	brittle temperature range;
CP	commercially pure;
DED	direct energy deposition;
DLD	direct laser deposition;
DMD	direct metal deposition;
DMLS™	Direct Metal Laser Sintering™;
FCC	face-centered cubic;
FGM	functionally graded material;
HIP	hot isostatic pressing;
LDED	laser directed energy deposition;
LENS™	Laser Engineered Net Shaping™;
LMD	laser metal deposition;
LPBF	laser powder bed fusion;
SLM	selective laser melting;
SLS	selective laser sintering;
SS	stainless steel.

Author details

Konstantin Makarenko*, Oleg Dubinin and Igor Shishkovsky
Skolkovo Institute of Science and Technology, Moscow, Russia

*Address all correspondence to: konstantin.makarenko@skoltech.ru

IntechOpen

References

[1] Lednev VN, Sdvizhenskii PA, Asyutin RD, Tretyakov RS, Grishin MY, Stavertiy AY, et al. In situ elemental analysis and failures detection during additive manufacturing process utilizing laser induced breakdown spectroscopy. Optics Express. 2019;**27**(4):4612-4628. DOI: 10.1364/OE.27.004612

[2] Tang Z, Liu W, Wang Y, Saleheen KM, Liu Z, Peng S, et al. A review on in situ monitoring technology for directed energy deposition of metals. The International Journal of Advanced Manufacturing Technology. 2020;**108**:3437-3463. DOI: 10.1007/s00170-020-05569-3

[3] Nasiri S, Khosravani MR. Machine learning in predicting mechanical behaviour of additively manufactured parts. Journal of Materials Research and Technology. 2021;**14**:1137-1153. DOI: 10.1016/j.jmrt.2021.07.004

[4] Grasso M, Remani A, Dickins A, Colosimo BM, Leach RK. In-situ measurement and monitoring methods for metal powder bed fusion: An updated review. Measurement Science and Technology. 2021;**32**:112001. DOI: 10.1088/1361-6501/ac0b6b

[5] Makarenko K, Dubinin O, Shornikov P, Shishkovsky I. Specific aspects of the transitional layer forming in the aluminium bronze – Stainless steel functionally graded structures after laser metal deposition. Procedia CIRP. 2020;**94**:346-351

[6] Onuike B, Heer B, Bandyopadhyay A. Additive manufacturing of Inconel 718-copper alloy bimetallic structure using laser engineered net shaping (LENS™). Additive Manufacturing. 2018;**21**:133-140. DOI: 10.1016/j.addma.2018.02.007

[7] Banait SM, Paul CP, Jinoop AN, Kumar H, Pawade RS, Bindra KS. Experimental investigation on laser directed energy deposition of functionally graded layers of Ni-Cr-B-Si and SS316L. Optics and Laser Technology. 2020;**121**:105787. DOI: j.optlastec.2019.105787

[8] Shishkovsky I, Kakovkina N, Scherbakov V. Fabrication of heat-resisting nickel composite gradient structures with TiC nano additive during powder bed fusion process. Procedia CIRP. 2018;**74**:68-71. DOI: j.procir.2018.08.032

[9] Li W, Karnati S, Kriewall C, Liou F, Newkirk J, Taminger KMB, et al. Fabrication and characterisation of a functionally graded material from Ti-6Al-4V to SS316 by laser metal deposition. Additive Manufacturing. 2017;**14**:95-104. DOI: 10.1016/j.addma.2016.12.006

[10] Reichardt A, Dillon RP, Borgonia JP, Shapiro AA, McEnerney BW, Momose T, et al. Development and characterization of Ti-6Al-4V to 304L stainless steel gradient components fabricated with laser deposition additive manufacturing. Materials & Design. 2016;**104**:404-413. DOI: 10.1016/j.matdes.2016.05.016

[11] Tan C, Zhou K, Ma W, Min L. Interfacial characteristic and mechanical performance of maraging steel-copper functional bimetal produced by selective laser melting based hybrid manufacture. Materials & Design. 2018;**155**:77-85. DOI: 10.1016/j.matdes.2018.05.064

[12] Tan C, Chew Y, Bi G, Wang D, Ma W, Yang Y, et al. Additive manufacturing of steel–copper functionally graded material with ultrahigh bonding strength. Journal of Materials Science and Technology. 2021;**72**:217-222. DOI: 10.1016/j.jmst.2020.07.044

[13] Pęska M, Karczewski K, Rzeszotarska M, Polański M. Direct synthesis of Fe-Al alloys from elemental powders using laser engineered net shaping. Materials. 2020;**13**(3):531. DOI: 10.3390/ma13030531

[14] Shishkovsky I, Missemer F, Smurov I. Direct Metal Deposition of Functional Graded Structures in Ti- Al System. 2012;**39**:382-391. DOI: 10.1016/ j.phpro.2012.10.052

[15] Ghanavati R, Naffakh-Moosavy H. Additive manufacturing of functionally graded metallic materials: A review of experimental and numerical studies. Journal of Materials Research and Technology. 2021;**13**: 1628-1664. DOI: 10.1016/j.jmrt. 2021.05.022

[16] Saleh B, Jiang J, Fathi R, Al-hababi T, Xu Q, Wang L, et al. 30 years of functionally graded materials: An overview of manufacturing methods, applications and future challenges. Composites Part B Engineering. 2020; **201**:108376. DOI: 10.1016/j. compositesb.2020.108376

[17] Heer B, Bandyopadhyay A. Compositionally graded magnetic-nonmagnetic bimetallic structure using laser engineered net shaping. Materials Letters. 2018;**216**:16-19. DOI: 10.1016/ j.matlet.2017.12.129

[18] Yan L, Chen Y, Liou F. Additive manufacturing of functionally graded metallic materials: A review of experimental and numerical studies. Journal of Materials Research and Technology. 2021;**13**:1628-1664. DOI: 10.1016/j.jmrt.2021.05.022

[19] Makarenko K, Dubinin O, Shishkovsky I. Analytical evaluation of the dendritic structure parameters and crystallization rate of laser-deposited Cu-Fe functionally graded materials. Materials. 2020;**13**:5665. DOI: 10.3390/ ma13245665

[20] Sun X, Hao W, Geng G, Ma T, Li Y. Solidification microstructure evolution of undercooled Cu-15 wt.% Fe alloy melt. Advances in Materials Science and Engineering. 2018;**2018**:6304518. DOI: 10.1155/2018/6304518

[21] Cao MM, Zhou ZM, Tang LW, et al. Research progress of high strength and high conductivity Cu-Fe alloy. Materials Guide: Nano and New Material Album. 2011;**25**:2. in Chinese

[22] Imada R, Fujiwara Y, Tsunashima S. Structure and giant magnetoresistance effect of Fe/Cu and FeCoNi/Cu multilayers. Journal of Applied Physics. 1997;**81**:8. DOI: 10.1063/1.364462

[23] Monchesky TL, Heinrich B, Urban R, Myrtle K, Klaua M, Kirschner J. Magnetoresistance and magnetic properties of Fe/Cu/Fe/GaAs(100). Physical Review B. 1999;**60**:10242. DOI: 10.1103/PhysRevB.60.10242

[24] Monchesky TL, Urban R, Heinrich B, Klaua M, Kirschner J. Giant magnetoresistance of Fe/Cu/Fe(001) trilayers grown directly on GaAs(001). Journal of Applied Physics. 2000;**87**(9): 5167-5169. DOI: 10.1063/1.373283

[25] Hedgcock FT, Muir WB, Raudorf TW, Szmidt R. Magnetoresistance and magnetization in Cu: Fe alloys below 4.2°K. Physical Review Letters. 1968;**20**:457. DOI: 10.1103/PhysRevLett.20.457

[26] Zhang X, Pan T, Flood A, Chen Y, Zhang Y, Liou F. Investigation of copper/stainless steel multi-metallic materials fabricated by laser metal deposition. Materials Science and Engineering A. 2021;**811**:141071. DOI: 10.1016/j.msea.2021.141071

[27] Zhang H, Chen Y, Pan T, Cui W, Li L, Liou F. Joining of copper and stainless steel 304L using direct metal deposition. In: Proceedings of the 30th Annual International Solid Freeform Fabrication

Symposium; 12–14 August 2019; Austin, TX. Austin: The University of Texas at Austin; 2019. pp. 388-403

[28] Prasad HS, Brueckner F, Volpp J, Kaplan AFH. Laser metal deposition of copper on diverse metals using green laser sources. The International Journal of Advanced Manufacturing Technology. 2020;**107**:1559-1568. DOI: 10.1007/s00170-020-05117-z

[29] Bai Y, Zhang J, Zhao C, Li C, Wang H. Dual interfacial characterization and property in multi-material selective laser melting of 316L stainless steel and C52400 copper alloy. Materials Characterization. 2020;**167**:110489. DOI: 10.1016/j.matchar.2020.110489

[30] Osipovich KS, Gurianov DA, Chumaevsky AV. Influence of 3D-printing parameters on bimetallic products manufacturing process of Cu-Fe system. IOP Conference Series: Materials Science and Engineering. 2021;**1079**:042089. DOI: 0.1088/1757-899X/1079/4/042089

[31] Liu M, Kumar A, Bukkapatnam S, Kuttolamadom M. A review of the anomalies in directed energy deposition (DED) Processes & Potential Solutions - part quality & defects. Procedia Manufacturing. 2021;**53**:507-518. DOI: 10.1016/j.promfg.2021.06.093

[32] Qi H, Mazumder J, Ki H. Numerical simulation of heat transfer and fluid flow in coaxial laser cladding process for direct metal deposition. Journal of Applied Physics. 2006;**100**(2):024903. DOI: 10.1063/1.2209807

[33] Laeng J, Stewart J, Liou FW. Laser metal forming processes for rapid prototyping – A review. International Journal of Production Research. 2000; **38**(16):3973-3996. DOI: 10.1080/00207540050176111

[34] Grigoryants AG. The Fundamentals of a Laser Treatment of Materials.

Moscow: Mashinostroenie Publishing; 1989. 301 p. ISBN: 5-217-00432-0

[35] Vedenov AA, Gladush GG. Physical Processes during Laser Treatment of Materials. Moscow: Energoatomisdat; 1985. p. 208

[36] Levchenko EB, Chernyakov AL. Instability of surface waves in a nonuniformly heated liquid. Zhournal Eksperimental'noy i Teoreticheskoy Fiziki. 1981;**51**(1):202-209

[37] Khosroshani EF, Heydari A, Mirzayi B, Shamkhali AN. A model to calculate concentration-dependent surface tension of binary systems. Fluid Phase Equilibria. 2016;**423**:34-42. DOI: 10.1016/j.fluid.2016.04.007

[38] Smith WG, Tiller WA, Rutter JW. Canadian Journal of Physics. 1955;**33**:723

[39] Chen YZ, Liu F, Yang GC, Xu XQ, Zhou YH. Rapid solidification of bulk undercooled hypoperitectic Fe–Cu alloy. Journal of Alloys and Compounds. 2007; **427**:L1-L5. DOI: 10.1016/j.jallcom.2006.03.012

[40] Wang CP, Liu XJ, Ohnuma I, Kainuma R, Ishida K. Thermodynamic database of the phase diagrams in Cu-Fe base ternary systems. Journal of Phase Equilibria and Diffusion. 2004;**25**: 320-328. DOI: 10.1007/s11669-004-0150-5

[41] Curiotto S, Greco R, Pryds NH, Johnson E, Battezzati L. The liquid metastable miscibility gap in Cu-based systems. Fluid Phase Equilibria. 2007; **256**:132-136. DOI: 10.1016/j.fluid.2006.10.003

[42] Chuang Y, Schmid R, Chang Y. Thermodynamic analysis of the iron-copper system I: The stable and metastable phase equilibria. Metallurgical Transactions A. 1984;**15**: 1921-1930. DOI: 10.1007/BF02664905

[43] Ma E, Atzmon M, Pinkerton FE. Thermodynamic and magnetic properties of metastable FexCu100−x solid solutions formed by mechanical alloying. Journal of Applied Physics. 1993;**74**:955. DOI: 10.1063/1.354837

[44] Raghavan V. Al-Cu-Fe (Aluminum-Copper-Iron). Journal of Phase Equilibria and Diffusion. 2005;**26**(1):59-64. DOI: 10.1361/15477030522509

[45] Raghavan V. Al-Cu-Fe (Aluminum-copper-iron). Journal of Phase Equilibria and Diffusion. 2010;**31**(5):449-452. DOI: 10.1361/15477030522509

[46] Chen HL, Du Y, Xu H, Xiong W. Experimental investigation and thermodynamic modeling of the ternary Al-Cu-Fe system. Journal of Materials Research. 2009;**24**(10):3154-3164. DOI: 10.1557/jmr.2009.0376

[47] Svetlizky D, Das M, Zheng B, Vyatskikh AL, Bose S, Bandyopadhyay A, et al. Directed energy deposition (DED) additive manufacturing: Physical characteristics, defects, challenges and applications. Materials Today. 2021;**49**:271-295. DOI: 10.1016/j.mattod.2021.03.020

[48] Kou S. Solidification and liquation cracking issues in welding. JOM. 2003;**55**:37-42. DOI: 10.1007/s11837-003-0137-4

[49] Wei HL, Mukherjee T, Zhang W, Zuback JS, Knapp GL, De A, et al. Mechanistic models for additive manufacturing of metallic components. Progress in Materials Science. 2021;**116**:100703. DOI: 10.1016/j.pmatsci.2020.100703

[50] Attalah MM, Jennings R, Wang X, Carter LN. Additive manufacturing of Ni-based superalloys: The outstanding issues. MRS Bulletin. 2016;**41**:758-764. DOI: 10.1557/mrs.2016.211

[51] Bi G, Gasser A. Restoration of Nickel-Base turbine blade knife-edges with controlled laser aided additive manufacturing. Physics Procedia. 2011;**12**:402-409. DOI: 10.1016/j.phpro.2011.03.051

[52] Ramirez AJ, Lippold JC. High temperature behavior of Ni-base weld metal part I. ductility and microstructural characterization. Materials Science and Engineering A. 2004;**380**:259-271. DOI: 10.1016/j.msea.2004.03.074

[53] Noecker FF, DuPont JN. Metallurgical investigation into ductility dip cracking in Ni-based alloys: Part I. Welding Journal. 2009;**88**(1):7s-20s

[54] Bahl S, Plotkowski A, Sisco K, Leonard DN, Allard LF, Michi RA, et al. Elevated temperature ductility dip in an additively manufactured Al-Cu-Ce alloy. Acta Materialia. 2021;**220**:117285. DOI: 10.1016/j.actamat.2021.117285

[55] Wang XH, Liu SS, Zhao GL, Zhang M, Ying WL. In-situ formation ceramic particles reinforced Fe-based composite coatings produced by ultrasonic assisted laser melting deposition processing. Optics and Laser Technology. 2021;**136**:106746. DOI: 10.1016/j.optlastec.2020.106746

[56] Todaro CJ, Easton MA, Qui D, Zhang D, Bermingham MJ, Lui EW, et al. Grain structure control during metal 3D printing by high-intensity ultrasound. Nature Communications. 2020;**11**:142. DOI: 10.1038/s41467-019-13874-z

[57] Zhang D, Li Y, Wang H, Cong W. Ultrasonic vibration-assisted laser directed energy deposition in-situ synthesis of NiTi alloys: Effects on microstructure and mechanical properties. Journal of Manufacturing Processes. 2020;**60**:328-339. DOI: 10.1016/j.jmapro.2020.10.058

[58] Espacenet Patent Search. KR101820719B1 DED Metal Reinforcement Method of Direct Energy Deposition Using Ultrasonic Wave Excitation [Internet]. 2018. Available from: https://worldwide.espacenet.com/patent/search/family/058742114/publication/KR101820719B1?q=pn%3DKR101820719B1 [Accessed: 2021-11-12]

[59] Zhang Y, Guo Y, Chen Y, Kang L, Cao Y, Qi H, et al. Ultrasonic-assisted laser metal deposition of the Al 4047Alloy. Metals. 2019;**9**:1111. DOI: 10.3390/met9101111

[60] Yan S, Wu D, Huang Y, Liu N, Zhang Y, Niu F, et al. C fiber toughening Al2O3-ZrO2 eutectic via ultrasonic-assisted directed laser deposition. Materials Letters. 2019;**235**: 228-231. DOI: 10.1016/j.matlet.2018.10.047

[61] Espacenet Patent Search. CN109604603A Ultrasonic-Assisted Laser-Deposition Additive Manufacturing Method and Device [Internet]. 2020. Available from: https://worldwide.espacenet.com/patent/search/family/066021766/publication/CN109604603A?q=pn%3DCN109604603A [Accessed: 2021-11-12]

[62] Gorunov AI. Development of the science and technological basics of creating materials with enhanced physicomechanical and exploitational properties via the DED [thesis]. Saint Petersburg: Peter the Great St. Petersburg Polytechnic University; 2021

[63] Zhang K, Wang S, Liu W, Shang X. Characterization of stainless steel parts by laser metal deposition shaping. Materials and Design. 2014;**55**:104-119. DOI: 10.1016/j.matdes.2013.09.006

[64] Guo P, Zou B, Huang C, Gao H. Study on microstructure, mechanical properties and machinability of efficiently additive manufactured AISI 316L stainless steel by high-power direct laser deposition. Journal of Materials Processing Technology. 2017;**240**:12-22. DOI: 10.1016/j.jmatprotec.2016.09.005

[65] Azinpour E, Darabi R, Cesar de Sa J, Santos A, Hodek J, Dzugan J. Fracture analysis in directed energy deposition (DED) manufactured 316L stainless steel using a phase-field approach. Finite Elements in Analysis and Design. 2020;**177**:103417. DOI: 10.1016/j.finel.2020.103417

[66] Stepinski T, Wu P. Evaluation of ultrasonic attenuation and estimation of ultrasonic grain noise in copper. AIP Conference Proceedings. 1999;**497**:431. DOI: 10.1063/1.1303084

[67] Riedel E, Liepe M, Scharf S. Simulation of ultrasonic induced cavitation and acoustic streaming in liquid and solidifying aluminum. Metals. 2020;**10**:476. DOI: 10.3390/met10040476

[68] Suslick KS, Neis U. The chemical effects of ultra-sound. Scientific American. 1989;**260**:80-86

[69] Shishkovsky I, Saphronov V. Peculiarities of selective laser melting process for permalloy powder. Materials Letters. 2016;**171**:208-211. DOI: 10.1016/j.matlet.2016.02.099

[70] Wang J, Wang Y, Shi J, Su Y. Effect of external magnetic field on the microstructure of 316L stainless steel fabricated by directed energy deposition. In: Proceedings of the International Mechanical Engineering Congress & Exposition; 11–14 November 2019. Salt Lake City. Utah: ASME; 2019. pp. 866-870. DOI: 10.1115/IMECE2019-12122

[71] Du D, Dong A, Shu D, Wang D, Zhu G, Sun B, et al. Influence of static magnetic field on the microstructure of nickel-based Superalloy by laser-

directed energy deposition. Metallurgical and Materials Transactions A. 2020;**51**:3354-3359. DOI: 10.1007/s11661-020-05783-4

[72] Du D, Haley JC, Dong A, Fautrelle Y, Shu D, Zhu G, et al. Influence of static magnetic field on microstructure and mechanical behavior of selective laser melted AlSi10Mg alloy. Materials & Design. 2019;**181**:107923. DOI: 10.1016/j.matdes.2019.107923

[73] Filimonov AM, Rogozin OA, Dubinin ON, Kuzminova YO, Shibalova AA, Okulov IV, et al. Modification of mechanical properties in directed energy deposition by a static magnetic field: Experimental and theoretical analysis. Materials. 2021;**14**:5190. DOI: 10.3390/ma14185190

[74] Smith PH, Murray JW, Jones DO, Segal J, Clare AT. Magnetically assisted directed energy deposition. Journal of Materials Processing Technology. 2021;**288**:116892. DOI: 10.1016/j.jmatprotec.2020.116892

[75] Smith PH, Murray JW, Jackson-Crisp A, Segal J, Clare AT. Magnetic manipulation in directed energy deposition using a programmable solenoid. Journal of Materials Processing Technology. 2022;**299**:117342. DOI: 10.1016/j.jmatprotec.2021.117342

[76] Dubinin ON, Chernodubov DA, Kuzminova YO, Shaysultanov DG, Akhatov IS, Stepanov ND, et al. Gradient soft magnetic materials produced by additive manufacturing from non-magnetic powders. Journal of Materials Processing Technology. 2022;**300**:117393. DOI: 10.1016/j.jmatprotec.2021.117393

[77] Du Plessis A, Macdonald E. Hot isostatic pressing in metal additive manufacturing: X-ray tomography reveals details of pore closure. Additive Manufacturing. 2020;**34**:101191. DOI: 10.1016/j.addma.2020.101191

[78] Molaei R, Fatemi A, Phan N. Significance of hot isostatic pressing (HIP) on multiaxial deformation and fatigue behaviours of additive manufactured Ti-6Al-4V including build orientation and surface roughness effects. International Journal of Fatigue. 2018;**117**:352-370. DOI: 10.1016/j.ijfatigue.2018.07.035

[79] Li P, Warner DH, Pegues JW, Roach MD, Shamsaei N, Phan N. Investigation of the mechanisms by which hot isostatic pressing improves the fatigue performance of powder bed fused Ti-6Al-4V. International Journal of Fatigue. 2019;**120**:342-352. DOI: 10.1016/j.ijfatigue.2018.10.015

[80] Tran TQ, Chinnappan A, Lee JKY, Loc NH, Tran LT, Wang G, et al. 3D printing of highly pure copper. Metals. 2019;**9**:756. DOI: 10.3390/met9070756

[81] Agarwala M, Bourell D, Beaman J, Marcus H, Barlow J. Post-processing of selective laser sintered metal parts. Rapid Prototyping Journal. 1995;**1**(2):36-44. DOI: 10.1108/13552549510086853

[82] Buffington FS, Hirano K, Cohen M. Self diffusion in iron. Acta Metallurgica. 1961;**9**(5):434-439. DOI: 10.1016/0001-6160(61)90137-7

[83] Kuper A, Letaw H Jr, Slifkin L, Sonder E, Tomizuka CT. Self-diffusion in copper. Physical Review. 1955;**98**:1870. DOI: 10.1103/PhysRev.96.1224

[84] Pavlov VA, Popov BV, Yakunin SN. Method of Hot Isostatic Pressing of Large Cylindrical Articles from Powders. Copyright Certificate [Internet]. 1989. Available from: https://www.elibrary.ru/item.asp?id=40585617 [Accessed: 2021-12-20]

[85] Foundry Management & Technology. World's Largest Hot Isostatic Press Again [Internet]. 2008. Available from: https://www.found

rymag.com/issues-and-ideas/article/
21925022/worlds-largest-hot-isostatic-
press-again [Accessed: 2021-12-19]

[86] Quintus Technologies. Hot Isostatic
Presses [Internet]. 2021. Available from:
https://quintustechnologies.com/
hot-isostatic-pressing/products/hot-
isostatic-presses [Accessed: 2021-12-18]

[87] Becker TH, Kumar P,
Ramamurty U. Fracture and fatigue in
additively manufactured metals. Acta
Materialia. 2021;**219**(33):117240. DOI:
10.1016/j.actamat.2021.117240

[88] Karakurt I, Ho KY, Ledford C,
Gamzina D, Horn T, Luhmann NC, et al.
Development of a magnetically driven
abrasive polishing process for additively
manufactured copper structures.
Procedia Manufacturing. 2018;**26**:
798-805. DOI: 10.1016/j.
promfg.2018.07.097

[89] Bai Y, Chaudhari A, Wang H.
Investigation on the microstructure and
machinability of ASTM A131 steel
manufactured by directed energy
deposition. Journal of Materials
Processing Technology. 2020;**276**:
116410. DOI: 10.1016/j.
jmatprotec.2019.116410